

Smart Construction of an Intimate Lithium | Garnet Interface for All-Solid-State Batteries by Tuning the Tension of Molten Lithium

Mingjie Du, Yang Sun, Bo Liu, Bingbing Chen, Kaiming Liao,* Ran Ran, Rui Cai, Wei Zhou, and Zongping Shao*

All-solid-state lithium batteries (ASSBs) have the potential to trigger a battery revolution for electric vehicles due to their advantages in safety and energy density. Screening of various possible solid electrolytes for ASSBs has revealed that garnet electrolytes are promising due to their high ionic conductivity and superior (electro)chemical stabilities. However, a major challenge of garnet electrolytes is poor contact with Li-metal anodes, resulting in an extremely large interfacial impedance and severe Li dendrite propagation. Herein, an innovative surface tension modification method is proposed to create an intimate Li | garnet interface by tuning molten Li with a trace amount of Si_3N_4 (1 wt%). The resultant Li-Si-N melt can not only convert the Li | garnet interface from point-to-point contact to consecutive face-to-face contact but also homogenize the electric-field distribution during the Li stripping/depositing process, thereby significantly decreasing its interfacial impedance ($1 \Omega \text{ cm}^2$ at 25°C) and improving its cycle stability (1000 h at 0.4 mA cm^{-2}) and critical current density (1.8 mA cm^{-2}). Specifically, the all-solid-state full cell paired with a LiFePO_4 cathode delivered a high capacity of 145 mAh g^{-1} at 2 C and maintained 97% of the initial capacity after 100 cycles at 1 C.

1. Introduction

Since the commercialization of the first rechargeable Li-ion battery (LIB) by Sony-Japan in the 1990s, significant academic and commercial progress has been made on LIBs. Recently, LIBs have started to power electric vehicles, but safety is a major concern, and high energy density is also required to meet an ever-increasing demand for long-distance travel.^[1] Conventional LIBs are limited by insufficient energy density and safety issues intrinsic to flammable liquid electrolytes.^[2] All-solid-state LIBs (ASSBs) with suitable solid-state electrolytes (SSEs) enable the use of the “Holy Grail” anode material of metallic Li (3860 mAh g^{-1} , -3.04 V vs SHE) and have been proposed and widely studied to improve the energy density and safety of the batteries.^[3] To date, various SSEs have been comprehensively explored for building high-performance ASSBs, including garnet,^[4] sulfide-based glass/ceramic,^[5] sodium superionic conductor

(NASICON),^[6] LiSICON,^[7] and perovskite materials.^[8] In particular, garnet SSEs (e.g., $\text{Li}_7\text{La}_3\text{Zr}_2\text{O}_{12}$, $\text{Li}_{6.5}\text{La}_3\text{Zr}_{1.5}\text{Nb}_{0.5}\text{O}_{12}$, $\text{Li}_{6.4}\text{La}_3\text{Zr}_{1.4}\text{Ta}_{0.6}\text{O}_{12}$) are highly attractive because of their good chemical stability in the presence of metallic Li, high Li-ion conductivity at room temperature (1 mS cm^{-1} for the state of the art), and wide electrochemical potential window ($\approx 0\text{--}5 \text{ V vs Li}^+/\text{Li}$) that enables matching with high voltage cathodes.^[9]


Despite the impressive merits offered by garnet SSEs, their targeted applications in ASSBs are limited by the high interfacial resistance originating from the poor contact of the garnet SSEs with metallic Li at the interface, even under hot pressing.^[10] Subsequently, the interface worsens during the latter repeated Li stripping process due to an increase in the number of voids, and contact loss occurs between the Li anode and the SSE, as illustrated in **Figure 1a**. It is generally accepted that interfacial contact also plays a critical role in regulating Li deposition.^[11] The poor contact at the interface accounts for a harmful point-to-point physical connection between the rigid garnet-SSE and the uneven Li metal anode, which causes an inhomogeneous Li-ion flux distribution during the Li plating/stripping process. Once Li dendrites nucleate and form, the local electrical field changes quickly.^[12] As a result, Li dendrites propagate in

M. Du, B. Liu, Prof. K. Liao, Prof. R. Ran, Prof. R. Cai,
Prof. W. Zhou, Prof. Z. Shao
State Key Laboratory of Materials-Oriented
Chemical Engineering
College of Chemical Engineering
Nanjing Tech University
Nanjing 210009, China
E-mail: kaimingliao@njtech.edu.cn; shaozp@njtech.edu.cn

Prof. Y. Sun
School of Materials
Sun Yat-sen University
Guangzhou 510006, China

Prof. B. Chen
School of Energy Science and Engineering
Nanjing Tech University
Nanjing 210009, China

Prof. Z. Shao
Department of Chemical Engineering
Curtin University
Perth, WA 6845, Australia

 The ORCID identification number(s) for the author(s) of this article can be found under <https://doi.org/10.1002/adfm.202101556>.

DOI: 10.1002/adfm.202101556

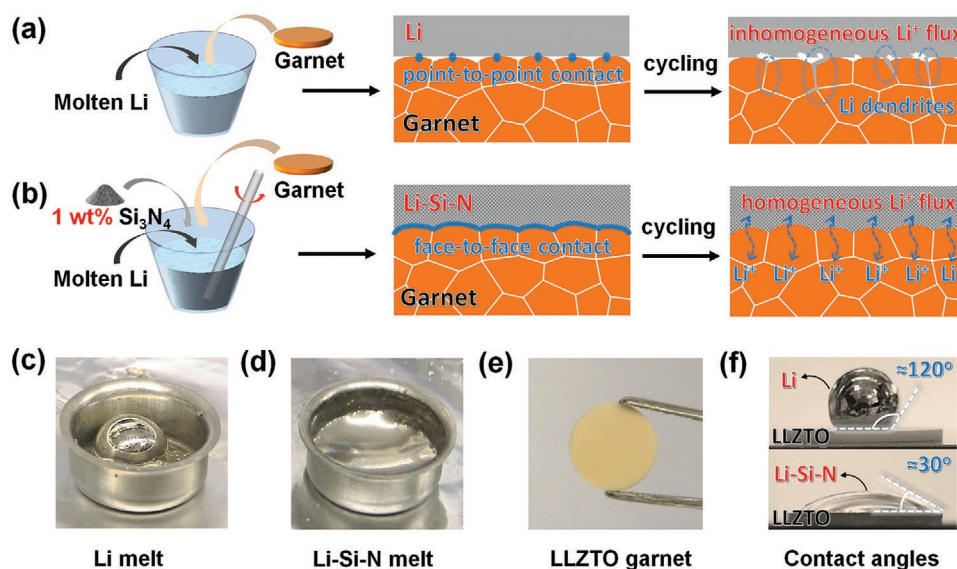


Figure 1. Schematic illustration showing the preparation of a) pure Li melt and b) Li-Si-N melt and the resultant interface contact behaviors with garnet pellets. Point-to-point interface contact is transformed into face-to-face contact with the help of 1 wt% Si_3N_4 modifier, enabling a dendrite-free system for better Li-ion transport across the interface. The digital photos show c) pure Li melt, d) Li-Si-N melt, e) LLZTO garnet pellet, and f) corresponding contact angles.

garnet SSEs even faster than in conventional liquid electrolytes, leading to a low critical current density (CCD) for the stable operation of Li metal electrodes and rapid short-circuiting of ASSBs.^[13] Therefore, improving the interfacial contact is not only significant for reducing the interfacial resistance but also important for suppressing Li dendrite formation.

Many efforts have been made to tailor the interfacial contact between garnet SSEs and Li metal electrodes to achieve a low interface impedance and enable dendrite-proof Li plating/stripping at a high CCD. Referring to previous reports, three main approaches have been highlighted: 1) Removing lithiophobic species from garnet SSEs. Recent experimental and computational studies have revealed that garnet SSEs are intrinsically lithiophilic, and that poor Li | garnet SSE interfaces arise because of the uncontrollable formation of lithiophobic contaminants (e.g., Li_2CO_3 and LiOH) on garnet SSE surfaces during air exposure.^[14] Many attempts have been made to remove surface contaminants, including rapid acid treatment,^[15] high-temperature carbon annealing,^[16] and thermal treatment at $>700^\circ\text{C}$.^[17] However, garnet SSEs treated by the methods mentioned above usually cause electronically conductive defects or loss of lithium. Meanwhile, regeneration of surface contaminants is inevitable if the garnet SSEs are re-exposed to the air. 2) Tailoring wettability of the molten Li. It is widely accepted that the poor wettability of molten Li does not allow it to spread across the surface of garnet SSEs due to the lithiophobic contaminants described above. Instead of removing surface contaminants, some research endeavors have been made to improve the wettability of molten Li by modifying the composition. Examples of these efforts include Li@50 wt% graphite,^[18] Li@50 wt% Na,^[19] Li@33 wt% Zn,^[20] Li@30 wt% Sn,^[21] and Li@10 wt% g- C_3N_4 .^[22] With all these efforts, the Li | garnet SSE interfacial resistance has been reduced to $5\ \Omega\ \text{cm}^2$. However, introducing additional material to the Li anode inevitably lowers the energy density of the whole battery; thus, the

additive amount should be as small as possible. 3) Introducing a buffer layer on garnet SSEs. Polymer electrolytes (PEO, PVDF),^[23] polymer films (PDMS, PAA, etc.),^[24] and inorganic thin films (BN, ZnO, Al_2O_3 , Cu_3N , SnN_x , Ge, Sn, Mg, C, Au, Ag, etc.)^[25,26] have been utilized to optimize the Li | garnet SSE interface. Although polymer-based buffer layers are flexible and soft and enable intimate contact with garnet SSEs, their Li-ion conductivity at room temperature is still insufficient. The practical use of inorganic thin films in ASSBs, however, is greatly hampered by manufacturing costs and technology (e.g., atomic layer deposition, chemical vapor deposition, electron beam thermal evaporation). Consequently, efforts to explore possible solutions for the Li | garnet SSE interface are still highly needed.

Herein, we report the construction of an intimate Li | garnet SSE interface that achieves ultralow interfacial impedance, fast charge-discharge rate, and long cycling life without showing signs of short-circuiting, as illustrated in Figure 1b. Our approach utilizes the chemical reaction between Si_3N_4 (1 wt%) and Li at 250°C to create a distinct Li-Si-N melt that easily spreads on the garnet SSE ($\text{Li}_{6.4}\text{La}_3\text{Zr}_{1.4}\text{Ta}_{0.6}\text{O}_{12}$, LLZTO) due to low surface tension. The contact angles of the pristine Li melt and the Li-Si-N melt on LLZTO pellets were greatly reduced from 120° to 30° . In addition, the in situ-formed Li_3N and LiSi_2N_3 species are good Li-ion conductors at the Li-Si-N | LLZTO interface, which can isolate electrical contact between the LLZTO and Li, thus effectively suppressing the formation of dendritic Li. Density functional theory (DFT) calculations revealed that the presence of Li_3N and LiSi_2N_3 in molten Li can effectively decrease the interface formation energy of Li | LLZTO. Owing to these merits, our solid-state Li-symmetric cells show much lower interfacial impedance ($1\ \Omega\ \text{cm}^2$ at 25°C) than other Li | garnet | Li cells reported to date. Moreover, this Li-Si-N melt demonstrates good applications in all-solid-state full batteries (e.g., Li-Si-N | LLZTO | LiFePO_4). A fundamental

understanding of intimate Li | garnet interface formation and outstanding electrochemical performance are further exploited.

2. Results and Discussion

The $\text{Li}_{6.4}\text{La}_3\text{Zr}_{1.4}\text{Ta}_{0.6}\text{O}_{12}$ (LLZTO) pellet was selected as the model garnet SSE for this study because of its high ionic conductivity at room temperature. It was prepared by a solid-state reaction according to procedures described in a previous report.^[26] The pure cubic phase (Figure S1, Supporting Information, PDF 45–0109) and high relative density (Figure S2, Supporting Information) resulted in ionic conductivity of the as-prepared LLZTO pellet as high as $8 \times 10^{-4} \text{ S cm}^{-1}$ at 25 °C (Figure S3, Supporting Information). The LLZTO pellets were mechanically polished to flatten the electrolyte and remove the surface contaminants (e.g., Li_2CO_3 and LiOH). The Li melt was obtained by heating pure Li foil at 250 °C in an Ar-filled glovebox. The Li-Si-N melt was prepared by simply adding 1 wt% Si_3N_4 powder (with a size of approximately 20 nm and a surface area of 46 m^2g^{-1} , Figure S4, Supporting Information) into molten Li in the same preparation process. Note that the Li melt shrank into a droplet in a stainless steel container (Figure 1c), but the Li-Si-N melt laid flat (Figure 1d). It is widely accepted that liquid droplets tend to gather into the smallest volume state to form the smallest possible spherical shape due to surface tension.^[27] Surface tension is related to the mutual attraction of liquid molecules, including the attraction of chemical bonds, hydrogen bonds, and van der Waals bonds. Usually, liquid-state metal shrinks easily because the

metal bond is a chemical bond, which is much stronger than hydrogen bonds and van der Waals bonds. Therefore, the different shrinkage states of the molten Li and Li-Si-N indicate a remarkable change in the surface tension with the addition of 1 wt% Si_3N_4 . To determine whether surface tension affected the contact mode of the molten Li and the Li-Si-N with the LLZTO pellet (Figure 1e), a contact angle test was performed. As shown in Figure 1f, the contact angles of the Li melt and the Li-Si-N melt on LLZTO pellets greatly decreased from approximately 120° to 30°, which further confirms that the Li-Si-N melt had a lower surface tension than the Li melt, thus enabling the Li-Si-N melt to spread well on the LLZTO garnet and provide intimate physical contact.

The X-ray diffraction (XRD) patterns in Figure 2a provide the phase information of the as-received Si_3N_4 , pristine Li foil, and the obtained Li-Si-N composite. For the pristine Li foil, two diffraction peaks at approximately 36.4° and 52.4° can be well indexed to the (110) and (200) planes of the cubic structure Li (PDF 15–0401). For the as-received Si_3N_4 powder, all diffraction peaks can be well-indexed to $\gamma\text{-Si}_3\text{N}_4$ (PDF 01-075-8455). After reaction with molten Li, the Si_3N_4 peaks completely (1 wt% Si_3N_4 , Figure S5, Supporting Information) or almost (20 wt% Si_3N_4 , Figure 2a) disappeared, and new diffraction peaks belonging to Li_3N , LiSi_2N_3 , and Li_xSi were detected in addition to the peaks of the Li metal in the Li-Si-N composite, indicating that the as-received Si_3N_4 powder completely reacted with molten Li. To achieve a fundamental understanding of the reaction between Si_3N_4 and Li, thermodynamic analysis based on DFT calculations were performed. Table S1, Supporting Information, lists all the possible reaction equations,

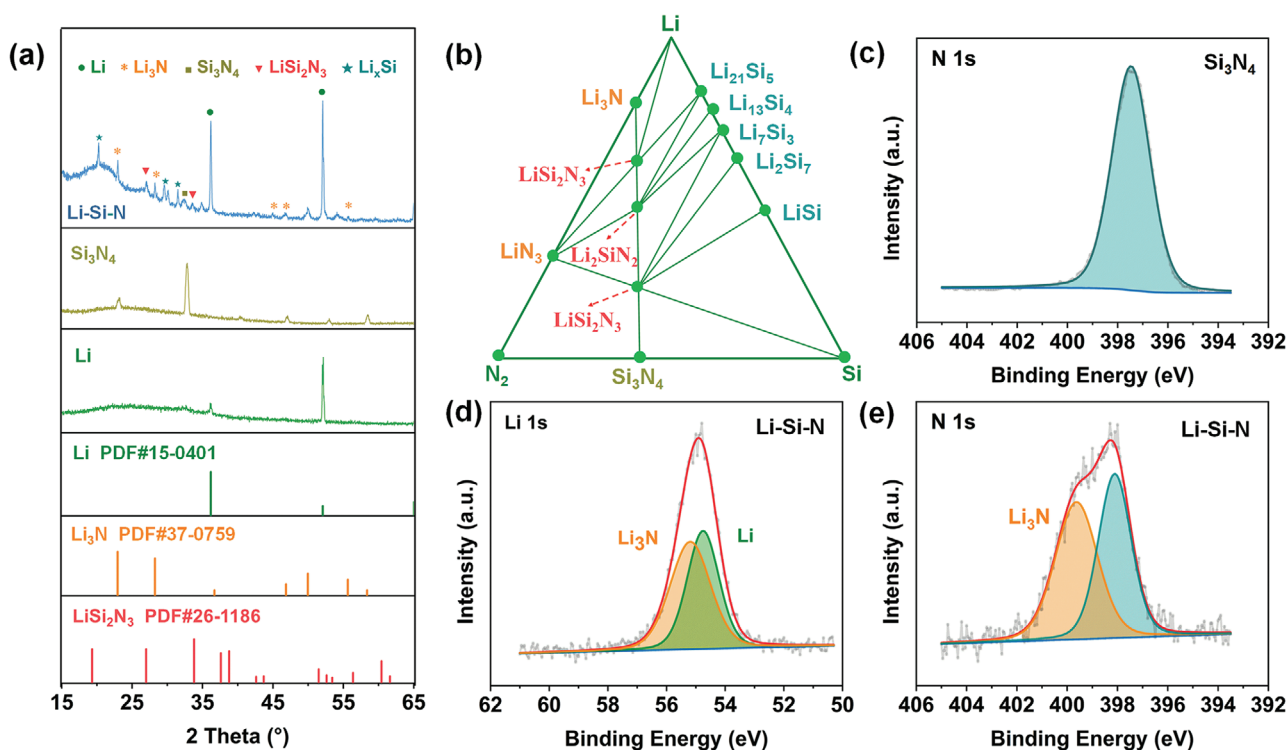


Figure 2. Characterization analysis of Li-Si-N composite. a) XRD patterns of the Li, Si_3N_4 , and Li-Si-N composite. b) Phase equilibrium diagram of the Li-Si-N system. c) N 1s XPS spectrum of Si_3N_4 . d,e) Li 1s and N 1s XPS data collected from the Li-Si-N composite.

in conjunction with the phase diagram of the Li-Si-N system (Figure 2b), suggesting that Li_3N , LiSi_2N_3 , and Li_xSi are instable phases in the final Li-Si-N composite. Therefore, the reaction $\text{Li} + \text{Si}_3\text{N}_4 \rightarrow \text{Li}_3\text{N} + \text{LiSi}_2\text{N}_3 + \text{Li}_x\text{Si}$ is proposed in light of its thermodynamic favorability. X-ray photoelectron spectroscopy (XPS) was carried out to acquire further information about the chemical state of the Li and N species in the Li-Si-N composite. As shown in Figure 2c, the N 1s spectrum of the as-received Si_3N_4 with a peak centered at 397.5 eV corresponding to the Si-N species.^[28] The Li 1s spectrum of the Li-Si-N composite (Figure 2d) can be fitted to two peaks centered at 54.8 and 55.2 eV, which can be assigned to Li and Li_3N , respectively. In addition, the XPS signal of the N 1s in the Li-Si-N composite (Figure 2e) can be fitted into two peaks centered at 400.0 and 398 eV, which correspond to Li-N and Si-N species, respectively.^[22] Based on DFT calculations and XRD and XPS analyses, the co-existence of Li metal, Li_3N , LiSi_2N_3 , and Li_xSi species in the Li-Si-N composite can be concluded.

The surface chemistry of the Li-Si-N composite was then investigated by DFT calculations. As shown in Figure 3a–c, the interfacial formation energies of Li | LLZTO, Li_3N | LLZTO, and LiSi_2N_3 | LLZTO were -0.97 , -1.47 , and -1.82 J m^{-2} , respectively, indicating that the interfacial formation energies of Li_3N | LLZTO and LiSi_2N_3 | LLZTO were more negative than those of Li | LLZTO. The data imply that the Li_3N and LiSi_2N_3 species generated from the reaction between Si_3N_4 and molten Li were beneficial for enhancing chemical contact between Li and LLZTO. The improved interfacial contact was further presented by cross-section scanning electron microscope (SEM) testing. As shown in Figure 3d–f and Figure S6, Supporting Information, the upper section of the image is the pure Li or Li-Si-N

composite, and the lower section is the LLZTO pellet. There was a large gap between the Li melt and the LLZTO pellet, while the Li-Si-N melt filled the surface voids of the LLZTO pellet and maintained close contact with the LLZTO particles. The difference in behavior of the melts demonstrates the effectiveness of the addition of Si_3N_4 in altering the interface contact between the Li and LLZTO garnet. The EDS mapping image of the Li-Si-N | LLZTO interface confirms that N (Figure 3g) was uniformly dispersed in the Li metal and maintained good contact with the La and Ta at the Li-Si-N | LLZTO interface, as shown in Figure 3h,i, which is in agreement with the SEM results. The overall investigation indicates that the construction of a Li | garnet interface with a Si_3N_4 additive proceeds via two major pathways: 1) lowering the surface tension of molten Li to enable it to easily spread on garnet pellets to achieve good physical contact and 2) decreasing the interfacial formation energy of Li | garnet to enhance the chemical contact between the Li and the garnet. The second method works only when there is a large amount of additive.^[18] However, introducing a large amount of additional material into the Li anode inevitably lowers the energy density of the whole battery. Therefore, this promising method demonstrated in this study is the first one smart construction of a stable and intimate Li | garnet interface created by lowering the surface tension of molten Li with a trace amount of Si_3N_4 (1 wt%).

To evaluate the interface resistance and the electrochemical stability of the Si_3N_4 -modified Li | garnet interface, symmetric cells of Li | LLZTO | Li and Li-Si-N | LLZTO | Li-Si-N were assembled. EIS tests were carried out prior to the CCD and cycling tests to evaluate the initial interfacial resistances. Figure 4a shows the Nyquist plots of the Li | LLZTO | Li and

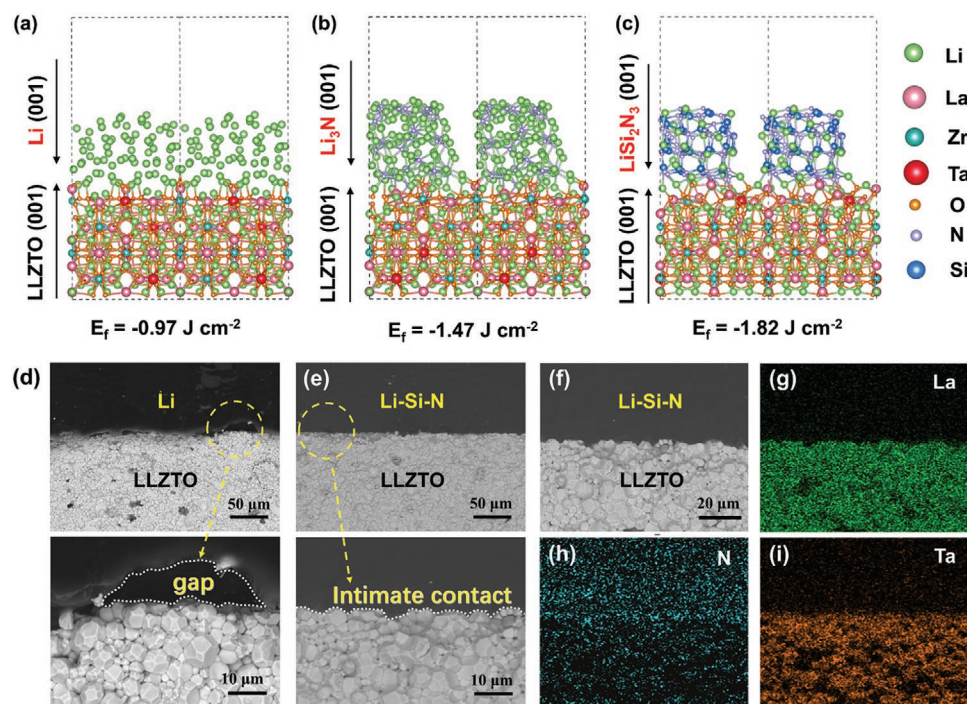


Figure 3. DFT calculations of the interfacial formation energies of the a) Li | LLZTO, b) Li_3N | LLZTO, and c) LiSi_2N_3 | LLZTO interfaces. SEM images of the cross-sections of the d) Li|LLZTO and e,f) Li-Si-N|LLZTO interfaces at different magnifications. g–i) EDS mapping analysis of the Li-Si-N|LLZTO interface.

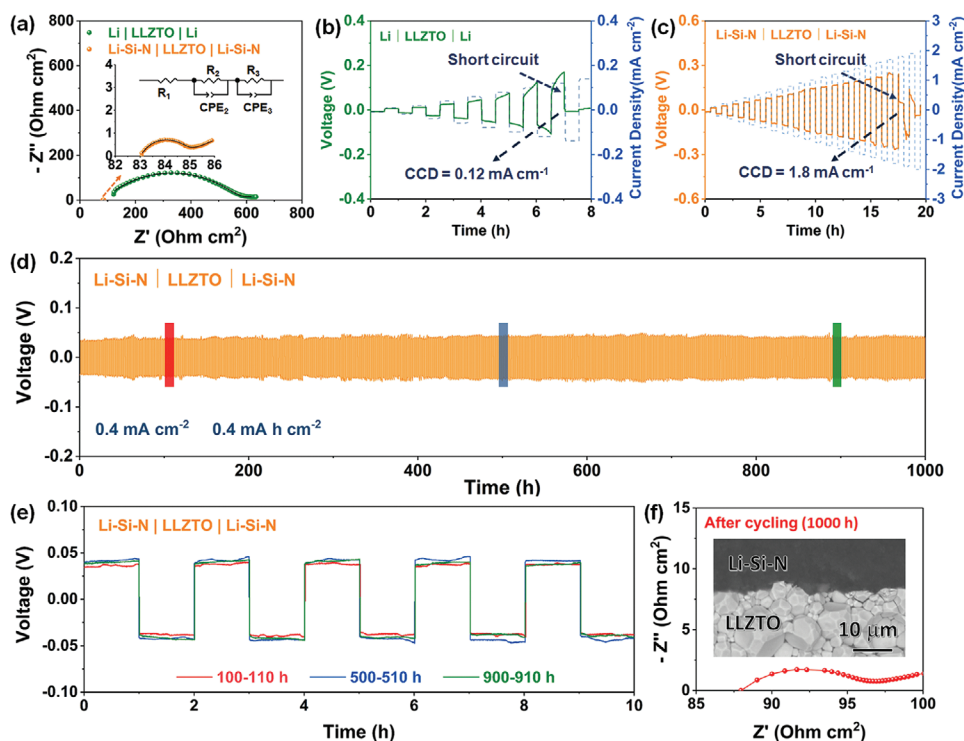


Figure 4. a) Comparison of EIS spectra of the Li | LLZTO | Li and Li-Si-N | LLZTO | Li-Si-N cells at room temperature. The inset shows corresponding equivalent circuit. b,c) Comparison of CCD of the Li | LLZTO | Li and Li-Si-N | LLZTO | Li-Si-N cells under step-increased current densities with upper limit set to 2 mA cm^{-2} . d,e) Li plating and stripping cycling of Li-Si-N | LLZTO | Li-Si-N cell under 0.4 mA cm^{-2} at room temperature and corresponding enlarged voltage profiles of Li plating/stripping at different cycling stages. f) EIS spectrum and cross-sectional SEM image of the Li-Si-N | LLZTO | Li-Si-N cell after being cycled at 0.4 mA cm^{-2} for 1000 h at room temperature.

Li-Si-N | LLZTO | Li-Si-N symmetric cells measured at room temperature. The semicircle in the Nyquist plot characterizes the electrode | electrolyte interface. The calculated area specific resistance (ASR) of the Li-Si-N | LLZTO | Li-Si-N cell is as small as $1 \Omega \text{ cm}^{-2}$ (referring to the one-sided electrode | electrolyte interface), which is a nearly 200-fold reduction in the value compared to the Li | LLZTO | Li cell ($220 \Omega \text{ cm}^{-2}$) and is also lower than some previously reported values for garnet electrolytes (Tables S2 and S3, Supporting Information). The CCD is defined as the maximum allowable current density at which the SSE can endure short circuits caused by Li dendrite penetration.^[13] Figure 4b,c compares the CCD of the symmetric cells with pristine Li and Li-Si-N composite electrodes. As expected, the Li-Si-N | LLZTO | Li-Si-N symmetric cell exhibited a high CCD of 1.8 mA cm^{-2} , while that of the Li | LLZTO | Li symmetric cell was only 0.12 mA cm^{-2} due to the poor interface contact. Additionally, galvanostatic cycling tests were performed to evaluate the long-term stability of Li | LLZTO and Li-Si-N | LLZTO interfaces. As shown in Figure S7, Supporting Information, the Li | LLZTO | Li symmetric cell showed a high overpotential of over 50 mV in the first cycle under testing conditions of 0.1 mA cm^{-2} and 0.1 mA h cm^{-2} , and a rapid short circuit occurred after cycling for 4 h. Note that the visible Li dendrites also appeared (Figure S8, Supporting Information), indicating an uneven Li plating/stripping process. This may have resulted from the fact that the poor contact of the Li | LLZTO interface forms a harmful point-to-point physical connection between the

lithium and the garnet, which causes a locally enhanced electric field and inhomogeneous Li-ion flux distribution during the Li plating/stripping process, accelerating dendrite growth. By contrast, long-term testing of Li-Si-N | LLZTO | Li-Si-N cells showed stable cycling performance for as long as 1000 h at 0.4 mA cm^{-2} (Figure 4d,e), 1500 h at 0.2 mA cm^{-2} (Figure S9, Supporting Information), and 300 h at 0.6 mA cm^{-2} (Figure S10, Supporting Information) without short circuiting or overpotential enlargement, demonstrating the superior interfacial stability and dendrite-suppressing capability of Li-Si-N composite electrodes, surpassing the performance described in most previous reports (as shown in Tables S2 and S3, Supporting Information). Moreover, only a slight increase in interfacial resistance ($4.5 \Omega \text{ cm}^2$) was detected even after the Li-Si-N | LLZTO | Li-Si-N cell was cycled for 1000 h at 0.4 mA cm^{-2} (Figure 4f), and the cross-sectional SEM image revealed that the Li-Si-N | LLZTO interface still maintained intimate contact after cycling for 1000 h (Figure 4f inset and Figure S11, Supporting Information), and without no signal of Li dendrites (Figure S8, Supporting Information). The above experimental results show that the Li-Si-N composite can not only achieve intimate interface contact with LLZTO garnet and reduce interface resistance but also significantly improve the CCD and stability of the Li-Si-N | LLZTO | Li-Si-N symmetric cell.

To further demonstrate the feasibility of the Li-Si-N | LLZTO interface, an all-solid-state full cell was assembled using LiFePO_4 as the cathode, an LLZTO pellet attached to Li-Si-N

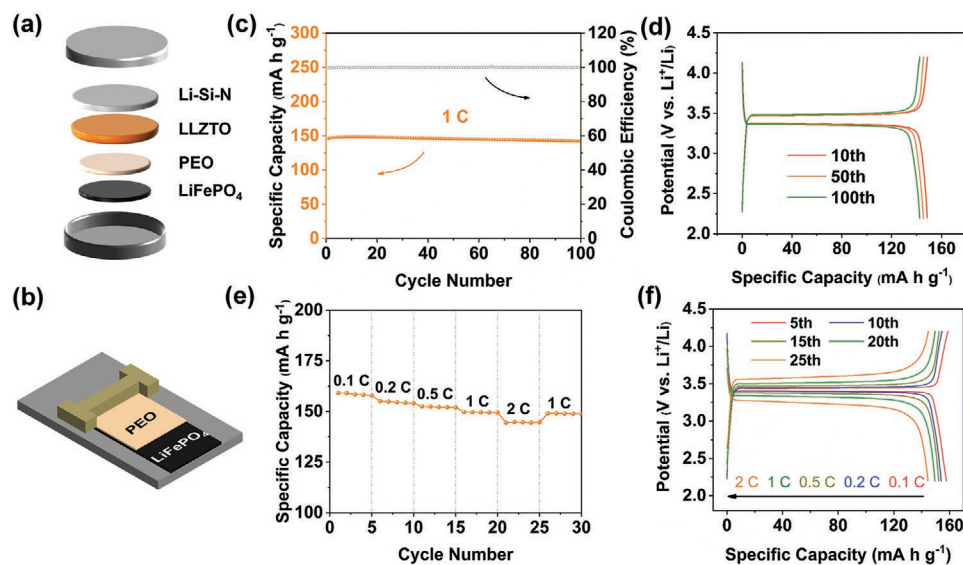


Figure 5. a,b) Schematic representation of the preparation and assembly of the all-solid-state Li-Si-N | LLZTO | PEO-LiFePO₄ cell. c,d) Cycle performance of the Li-Si-N | LLZTO | PEO-LiFePO₄ cell under 1 C at 60 °C and the typical charge-discharge voltage profiles with cycle numbers indicated. e,f) Rate performance and corresponding charge-discharge voltage profiles of the all-solid-state Li-Si-N | LLZTO | PEO-LiFePO₄ cell.

as the electrolyte and anode, and a PEO-based membrane as a cathode functional layer, as schematically illustrated in Figure 5a,b. The LiFePO₄ cathode with a loading of 2 mg cm⁻² was prepared by mixing the LiFePO₄ powder with Super P and a polymer (PEO₂₀-LiTFSI). Then, a PEO precursor solution (PEO₂₀-LiTFSI-10 wt% LLZTO-acetonitrile) was coated on the LiFePO₄ cathode, followed by heating evaporation to form a functional layer with a thickness of 12 μm (Figure S12, Supporting Information); see “Cell fabrication” in the Supporting Information. The soft PEO-based cathode functional layer possessed a high ionic conductivity of 1×10^{-3} S cm⁻¹ at 60 °C and a wide electrochemical potential window up to 4.2 V versus Li/Li⁺ at room temperature (Figure S13, Supporting Information), enabling the formation of an intimate cathode | electrolyte interface that reduced the resistance of Li⁺ migration across the interface. As expected, the all-solid-state Li-Si-N | LLZTO | PEO-LiFePO₄ full cell showed a total resistance of approximately 180 Ω cm² at 60 °C, which is much smaller than that of the Li | LLZTO | PEO-LiFePO₄ full cell (780 Ω cm², see Figure S14a, Supporting Information). The all-solid-state full cell delivered a high specific capacity of 146 mAh g⁻¹ at 1 C (Figure 5c) with small overpotentials exhibiting well-defined charge/discharge plateaus of approximately 3.4 V at a current density of 1 C (Figure 5d), which is even comparable to the performance of liquid-electrolyte LIBs. By contrast, the Li | LLZTO | PEO-LiFePO₄ full cell delivers a low discharge capacity of 115.5 mAh g⁻¹ for the first cycle, and following a rapid capacity fading after 10 cycles (Figure S14b, Supporting Information). In addition, the full cell maintained 97% of the initial capacity at 1 C for over 100 cycles with a high Coulombic efficiency of 99.9% (Figure 5c), suggesting superior cycling stability. Moreover, the all-solid-state Li-Si-N | LLZTO | LiFePO₄ full cell showed good rate performance ranging from 0.1 to 2 C. As shown in Figure 5e,f, the discharge capacities were 159, 155, 152, 150, and 145 mAh g⁻¹ at rates of 0.1, 0.2, 0.5, 1, and 2 C, respectively.

When the rate returned to 1 C, the specific capacity quickly recovered to 149 mAh g⁻¹. Therefore, the present results pave the way for the creation of high-capacity and high-rate ASSBs based on garnet-structured SSEs.

3. Conclusions

In summary, we provide the first demonstration of modifying the Li | garnet interface by tuning the surface tension of molten Li with a trace amount of nano Si₃N₄ (1 wt%). From the phase diagram of Li-Si-N systems, in conjunction with XRD and XPS analyses, the formation of Li₃N, LiSi₂N₃, and Li_xSi species was confirmed when heating a mixture of 1 wt% Si₃N₄ and Li metal, and the resultant composite was denoted as Li-Si-N melt. The Li-Si-N melt greatly improved the interfacial contact with garnet in two ways: 1) lowering the surface tension of molten Li to enable it to easily spread on garnet pellets to achieve superior physical contact and 2) decreasing the interfacial formation energy of Li | garnet to endow it with good chemical contact. Lowering the surface tension with 1 wt% Si₃N₄ played a dominant role. As expected, the contact angles of the pristine Li melt and the Li-Si-N melt on LLZTO pellets were approximately 120° and 30°, respectively. SEM images show that introducing 1 wt% Si₃N₄ into molten Li changed the Li | LLZTO interface from point-to-point contact to intimate face-to-face contact, enabling a homogeneous current distribution during the Li plating/stripping process. DFT calculations demonstrated that the Li₃N and LiSi₂N₃ species in molten Li can simultaneously reduce the interface formation energy of Li | LLZTO. As a result, the modified solid-state Li | LLZTO interface achieved an ultralow interfacial impedance of 1 Ω cm² at 25 °C and a high CCD of 1.8 mA cm⁻². After continuous charging and discharging at 0.4 mA cm⁻² for 1000 h, no dendritic Li penetration into the electrolyte layer was observed. Moreover, the all-solid-state

Li-Si-N | LLZTO | LiFePO₄ full cell could deliver a high capacity of 145 mAh g⁻¹ at 2 C and maintain 97% of the initial capacity after 100 cycles at 1 C. Therefore, our research provides new insights into a new class of molten Li anodes with tunable surface tension that can promote unfettered development of garnet-based ASSBs.

Supporting Information

Supporting Information is available from the Wiley Online Library or from the author.

Acknowledgements

This work was financially supported by the National Key R&D Program of China (No. 2018YFB0905400), National Natural Science Foundation of China (No. 51802152), and the Natural Science Foundation of Jiangsu Province of China (No. BK20170974).

Conflict of Interest

The authors declare no conflict of interest.

Author Contributions

M.J.D. carried out experiments. Y.S. conducted theoretical calculations to explain the interface formation energy. K.M.L. designed the experiments and wrote the manuscript. Z.P.S. participated in review and supervision. All authors contributed to the discussion and interpretation of the results.

Data Availability Statement

Research data are not shared.

Keywords

cycling stability, garnet electrolytes, interfacial impedance, Li depositing, solid batteries

Received: February 13, 2021

Revised: March 29, 2021

Published online:

- [1] a) M. Du, K. Liao, Q. Lu, Z. Shao, *Energy Environ. Sci.* **2019**, *12*, 1780; b) M. S. Whittingham, *Chem. Rev.* **2014**, *114*, 11414; c) X. Shen, R. Zhang, X. Chen, X. B. Cheng, X. Li, Q. Zhang, *Adv. Energy Mater.* **2020**, *10*, 1903645; d) E. Wang, Y. Zhao, D. Xiao, X. Zhang, T. Wu, B. Wang, M. Zubair, Y. Li, X. Sun, H. Yu, *Adv. Mater.* **2020**, *32*, 1906070; e) Y. Chu, Y. Shen, F. Guo, X. Zhao, Q. Dong, Q. Zhang, W. Li, H. Chen, Z. Luo, L. Chen, *Electrochem. Energy Rev.* **2020**, *3*, 187.
- [2] a) K. Liao, S. Wu, X. Mu, Q. Lu, M. Han, P. He, Z. Shao, H. Zhou, *Adv. Mater.* **2018**, *30*, 1705711; b) J. Yu, Y. Q. Lyu, J. Liu, M. B. Effat, S. C. T. Kwok, J. Wu, F. Ciucci, *J. Mater. Chem. A* **2019**, *7*, 17995;

- c) L. Zhang, T. Qian, X. Zhu, Z. Hu, M. Wang, L. Zhang, T. Jiang, J. H. Tian, C. Yan, *Chem. Soc. Rev.* **2019**, *48*, 5432; d) Z. Cheng, M. Liu, S. Ganapathy, C. Li, Z. Li, X. Zhang, P. He, H. Zhou, M. Wagemaker, *Joule* **2020**, *4*, 1311; e) Y. Zhang, B. Chen, D. Guan, M. Xu, R. Ran, M. Ni, W. Zhou, R. O'Hayre, Z. Shao, *Nature* **2021**, *591*, 246; f) X. Yang, K. R. Adair, X. Gao, X. Sun, *Energy Environ. Sci.* **2021**, *14*, 643.
- [3] a) T. Famprikis, P. Canepa, J. A. Dawson, M. S. Islam, C. Masquelier, *Nat. Mater.* **2019**, *18*, 1278; b) X. Gao, X. Yang, K. Adair, J. Liang, Q. Sun, Y. Zhao, R. Li, T. K. Sham, X. Sun, *Adv. Funct. Mater.* **2020**, *30*, 2005357; c) Q. Zhao, S. Stalin, C. Z. Zhao, L. A. Archer, *Nat. Rev. Mater.* **2020**, *5*, 229; d) F. Ye, K. Liao, R. Ran, Z. Shao, *Energy Fuels* **2020**, *34*, 194; e) X. Yang, Q. Sun, C. Zhao, X. Gao, K. Adair, Y. Zhao, J. Luo, X. Lin, J. Liang, H. Huang, L. Zhang, S. Lu, R. Li, X. Sun, *Energy Storage Mater.* **2019**, *22*, 194; f) X. Yang, X. Gao, S. Mukherjee, K. Doyle-Davis, J. Fu, W. Li, Q. Sun, F. Zhao, M. Jiang, Y. Hu, H. Huang, L. Zhang, S. Lu, R. Li, T. K. Sham, C. V. Singh, X. Sun, *Adv. Energy Mater.* **2020**, *10*, 2001191.
- [4] a) A. J. Samson, K. Hofstetter, S. Bag, V. Thangadurai, *Energy Environ. Sci.* **2019**, *12*, 2957; b) V. Thangadurai, S. Narayanan, D. Pinzaru, *Chem. Soc. Rev.* **2014**, *43*, 4714; c) M. Jia, N. Zhao, H. Huo, X. Guo, *Electrochem. Energy Rev.* **2020**, *3*, 656.
- [5] a) F. Zhao, S. H. Alahakoon, K. Adair, S. Zhang, W. Xia, W. Li, C. Yu, R. Feng, Y. Hu, J. Liang, X. Lin, Y. Zhao, X. Yang, T. K. Sham, H. Huang, L. Zhang, S. Zhao, S. Lu, Y. Huang, X. Sun, *Adv. Mater.* **2021**, *33*, 2006577; b) J. Wu, S. Liu, F. Han, X. Yao, C. Wang, *Adv. Mater.* **2021**, *33*, 2000751.
- [6] H. Y. P. Hong, J. B. Goodenough, J. A. Kafalas, *Mater. Res. Bull.* **1976**, *11*, 203.
- [7] A. R. Rodger, J. Kuwano, A. R. West, *Solid State Ionics* **1895**, *15*, 185.
- [8] a) Y. Li, W. Zhang, Y. Zheng, J. Chen, B. Yu, Y. Chen, M. Liu, *Chem. Soc. Rev.* **2017**, *46*, 6345; b) Z. Jiang, H. Xie, S. Wang, X. Song, X. Yao, H. Wang, *Adv. Energy Mater.* **2018**, *8*, 1801433.
- [9] a) Y. Gao, S. Sun, X. Zhang, Y. Liu, J. Hu, Z. Huang, M. Gao, H. Pan, *Adv. Funct. Mater.* **2021**, *31*, 2009692; b) Y. N. Yang, Y. X. Li, Y. Q. Li, T. Zhang, *Nat. Commun.* **2020**, *11*, 5519; c) H. Zheng, S. Wu, R. Tian, Z. Xu, H. Zhu, H. Duan, H. Liu, *Adv. Funct. Mater.* **2019**, *30*, 1906189; d) F. Fu, Y. Zhu, X. He, Y. Mo, C. Wang, *Adv. Energy Mater.* **2016**, *6*, 1502496; e) W. D. Richards, L. J. Miara, Y. Wang, J. C. Kim, G. Ceder, *Chem. Mater.* **2016**, *28*, 266; f) Y. Zhu, X. He, Y. Mo, *J. Mater. Chem. A* **2016**, *4*, 3253.
- [10] a) R. Chen, A. M. Nolan, J. Lu, J. Wang, X. Yu, Y. Mo, L. Chen, X. Huang, H. Li, *Joule* **2020**, *4*, 812; b) C. Yu, S. Ganapathy, E. Eck, H. Wang, S. Basak, Z. Li, M. Wagemaker, *Nat. Commun.* **2017**, *8*, 1086; c) Z. Shen, W. Zhang, G. Zhu, Y. Huang, Q. Feng, Y. Lu, *Small Methods* **2019**, *4*, 1900592; d) Y. Zhao, K. Zheng, X. Sun, *Joule* **2018**, *2*, 2583.
- [11] a) W. L. Huang, N. Zhao, Z. J. Bi, C. Shi, X. X. Guo, L. Z. Fan, C. W. Nan, *Mater. Today Nano* **2020**, *10*, 100075; b) Y. Song, L. Yang, L. Tao, Q. Zhao, Z. Wang, Y. Cui, H. Liu, Y. Lin, F. Pan, *J. Mater. Chem. A* **2019**, *7*, 22898; c) M. J. Wang, R. Choudhury, J. Sakamoto, *Joule* **2019**, *3*, 2165; d) J. Meng, Y. Zhang, X. Zhou, M. Lei, C. Li, *Nat. Commun.* **2020**, *11*, 3716.
- [12] a) X. Fu, T. Wang, W. Shen, M. Jiang, Y. Wang, Q. Dai, D. Wang, Z. Qiu, Y. Zhang, K. Deng, Q. Zeng, N. Zhao, X. Guo, Z. Liu, J. Liu, Z. Peng, *Adv. Mater.* **2020**, *32*, 2000575; b) P. Shi, X. Q. Zhang, X. Shen, B. Q. Li, R. Zhang, L. P. Hou, Q. Zhang, *Adv. Funct. Mater.* **2020**, *31*, 2004189; c) T. Krauskopf, R. Dippel, H. Hartmann, K. Peppeler, B. Mogwitz, F. H. Richter, W. G. Zeier, J. Janek, *Joule* **2019**, *3*, 2030; d) Y. Zhang, J. Meng, K. Chen, Q. Wu, X. Wu, C. Li, *ACS Appl. Mater. Interfaces* **2020**, *12*, 33729.
- [13] a) A. Sharafi, E. Kazyak, A. L. Davis, S. Yu, T. Thompson, D. J. Siegel, N. P. Dasgupta, J. Sakamoto, *Chem. Mater.* **2017**, *29*, 7961; b) H. Huo, Y. Chen, R. Li, N. Zhao, J. Luo, J. G. Pereira da Silva, R. Mücke, P. Kaghazchi, X. Guo, X. Sun, *Energy Environ. Sci.*

- 2020, 13, 127; c) H. Duan, M. Fan, W. P. Wang, L. Yu, S. J. Tan, X. Chen, Q. Zhang, S. Xin, L. J. Wan, Y. G. Guo, *Angew. Chem., Int. Ed.* **2020**, 59, 12069.
- [14] a) L. Cheng, E. J. Crumlin, W. Chen, R. Qiao, H. Hou, S. F. Lux, V. Zorba, R. Russo, R. Kostecki, Z. Liu, K. Persson, W. Yang, J. Cabana, T. Richardson, G. Chen, M. Doeff, *Phys. Chem. Chem. Phys.* **2014**, 16, 18294; b) A. Sharafi, S. Yu, M. Naguib, M. Lee, C. Ma, H. M. Meyer, J. Nanda, M. Chi, D. J. Siegel, J. Sakamoto, *J. Mater. Chem. A* **2017**, 5, 13475.
- [15] a) H. Huo, Y. Chen, N. Zhao, X. Lin, J. Luo, X. Yang, Y. Liu, X. Guo, X. Sun, *Nano Energy* **2019**, 61, 119; b) Y. Ruan, Y. Lu, Y. Li, C. Zheng, J. Su, J. Jin, T. Xiu, Z. Song, M. E. Badding, Z. Wen, *Adv. Funct. Mater.* **2020**, 31, 2007815.
- [16] Y. Li, X. Chen, A. Dolocan, Z. Cui, S. Xin, L. Xue, H. Xu, K. Park, J. B. Goodenough, *J. Am. Chem. Soc.* **2018**, 140, 6448.
- [17] J. F. Wu, B. W. Pu, D. Wang, S. Q. Shi, N. Zhao, X. Guo, X. Guo, *ACS Appl. Mater. Interfaces* **2019**, 11, 898.
- [18] J. Duan, W. Wu, A. M. Nolan, T. Wang, J. Wen, C. Hu, Y. Mo, W. Luo, Y. Huang, *Adv. Mater.* **2019**, 31, 1807243.
- [19] Y. Zhang, J. Meng, K. Chen, H. Wu, J. Hu, C. Li, *ACS Energy Lett.* **2020**, 5, 1167.
- [20] G. V. Alexander, O. V. Sreejith, M. S. Indu, R. Murugan, *ACS Appl. Energy Mater.* **2020**, 3, 9010.
- [21] C. Wang, H. Xie, L. Zhang, Y. Gong, G. Pastel, J. Dai, B. Liu, E. D. Wachsman, L. Hu, *Adv. Energy Mater.* **2018**, 8, 1701963.
- [22] Y. Huang, J. Duan, F. Yang, T. R. Wang, Z. F. Wang, W. J. Yang, C. C. Hu, W. Luo, Y. H. Huang, *Angew. Chem., Int. Ed.* **2020**, 59, 3699.
- [23] a) Y. Li, B. Xu, H. Xu, H. Duan, X. Lu, S. Xin, W. Zhou, L. Xue, G. Fu, A. Manthiram, J. B. Goodenough, *Angew. Chem., Int. Ed.* **2017**, 56, 753; b) B. Liu, Y. Gong, K. Fu, X. Han, Y. Yao, G. Pastel, C. Yang, H. Xie, E. D. Wachsman, L. Hu, *ACS Appl. Mater. Interfaces* **2017**, 9, 18809.
- [24] a) X. Zhang, Q. Xiang, S. Tang, A. Wang, X. Liu, J. Luo, *Nano Lett.* **2020**, 20, 2871; b) H. Huo, J. Gao, N. Zhao, D. Zhang, N. G. Holmes, X. Li, Y. Sun, J. Fu, R. Li, X. Guo, X. Sun, *Nat. Commun.* **2021**, 12, 176.
- [25] a) S. Rajendran, N. K. Thangavel, K. Mahankali, L. M. R. Arava, *ACS Appl. Energy Mater.* **2020**, 3, 6775; b) G. V. Alexander, S. Patra, S. V. S. Raj, M. K. Sugumar, M. M. Ud Din, R. Murugan, *J. Power Sources* **2018**, 396, 764; c) W. Feng, X. Dong, X. Zhang, Z. Lai, P. Li, C. Wang, Y. Wang, Y. Xia, *Angew. Chem., Int. Ed.* **2020**, 59, 5346; d) Y. Shao, H. Wang, Z. Gong, D. Wang, B. Zheng, J. Zhu, Y. Lu, Y. S. Hu, X. Guo, H. Li, X. Huang, Y. Yang, C. W. Nan, L. Chen, *ACS Energy Lett.* **2018**, 3, 1212; e) C. Wang, K. Fu, S. P. Kammampata, D. W. McOwen, A. J. Samson, L. Zhang, G. T. Hitz, A. M. Nolan, E. D. Wachsman, Y. Mo, V. Thangadurai, L. Hu, *Chem. Rev.* **2020**, 120, 4257.
- [26] K. Shi, L. Yang, Y. W. Zhang, Y. F. Huang, S. M. Su, H. F. Xia, K. L. Jiang, L. Shen, Y. Hu, S. Q. Zhang, J. Yu, F. Z. Ren, Y. B. He, F. Y. Kang, *Angew. Chem., Int. Ed.* **2020**, 59, 11784.
- [27] J. Wang, H. Wang, J. Xie, A. Yang, A. Pei, C. Wu, F. Shi, Y. Liu, D. Lin, Y. Gong, Y. Cui, *Energy Storage Mater.* **2018**, 14, 345.
- [28] Z. Xiao, C. Lei, C. Yu, X. Chen, Z. Zhu, H. Jiang, F. Wei, *Energy Storage Mater.* **2020**, 24, 565.